

Frequency-mixing spectroscopy of spins in diamond

Mohammed Attrash^{ID}, Sergei Masis^{ID}, Sergey Hazanov^{ID}, Oleg Shtempluck, and Eyal Buks^{ID*}

Andrew and Erna Viterbi Department of Electrical Engineering, Technion, Haifa 32000, Israel



(Received 26 June 2023; revised 11 September 2023; accepted 16 October 2023; published 1 November 2023)

Frequency-mixing processes in spin systems have a variety of applications in meteorology and in quantum data processing. Spin spectroscopy based on frequency mixing offers some advantages, including the ability to eliminate crosstalk between driving and detection. We experimentally explore nonlinear frequency-mixing processes with negatively charged nitrogen-vacancy defects in diamond at low temperatures, and near level anticrossing. The experimental setup allows simultaneously applying magnetic driving in the longitudinal and transverse directions. Magnetic resonance detection is demonstrated using both Landau-Zener-Stückelberg interferometry and two-tone driving spectroscopy. The experimental results are compared with predictions of a theoretical analysis based on the rotating wave approximation.

DOI: 10.1103/PhysRevApplied.20.054001

I. INTRODUCTION

Spins are essentially the most nonlinear systems found in nature. Their magnetic resonance is widely employed for sensing and imaging applications. In some cases, nonlinear response impacts the sensitivity and bandwidth of magnetic resonance imaging systems [1,2]. Nonlinear response can be exploited for performance enhancement in some cases. One example is enhancement of magnetic resonance detection sensitivity that is achieved using squeezed microwave fields [3]. Another example is driving-induced enhancement of coupling between spins [4]. Moreover, for quantum data processing, nonlinear response is an essential resource enabling the generation of entangled states [5] and topological frequency conversion [6]. In addition, nonlinear response of driven spins can be exploited for the generation of exotic states of matter by means of Floquet engineering [7].

Frequency-mixing processes that are enabled by nonlinear response can be employed for a variety of applications. In spectroscopy, sensitivity is commonly limited by crosstalk, when both driving and detection are performed at the same frequency (which is usually the case in cavity-based spectroscopy [2]). This problem can be avoided by employing frequency mixing, which enables resonance driving using only off-resonance driving tones. Other examples for frequency-mixing applications are electromagnetically induced transparency [8] and hole burning [9]. Frequency mixing can be used to manipulate transition rates between quantum states, which, in turn, can enable the control of states' population. Cooling induced by frequency mixing has been demonstrated in Ref. [10]

using a Josephson flux qubit. A similar process of frequency mixing can be implemented to achieve population inversion.

Here we explore frequency-mixing processes in negatively charged nitrogen-vacancy ($N-V^-$) defects in diamond at low temperatures. A $N-V^-$ defect has a spin triplet ground state with magnetic quantum numbers $m_S \in \{-1, 0, 1\}$ [11]. The $N-V^-$ electronic spin state can be polarized and read out with light in the optical band. Dense ensembles of $N-V^-$ defects were demonstrated to be applicable for magnetometry [12], for classical [13] and quantum [14–17] information storage, and for a maser implementation [18]. The $N-V$ magnetometry sensitivity may reach sub-pT Hz^{-1/2} level [19–21]. Dual driving of $N-V^-$ electrons and nuclear spins was investigated by optical detection of magnetic resonance (ODMR) [21–27], Landau-Zener-Stückelberg interferometry [28, 29], and electron-spin double resonance [1,30].

In this work we explore mixing between longitudinal driving in the radio-frequency (rf) band and transverse driving in the microwave (MW) band. To account for our experimental results, theoretical predictions derived using the rotating wave approximation (RWA) are presented. We find relatively strong nonlinear response near the $N-V^-$ ground-state level anticrossing (GSLAC) [9,25,26,31,32]. The response enhancement is attributed to a significant state mixing occurring near GSLAC. The same state mixing gives rise to a significant modification in transition selection rules. In particular, the commonly forbidden transition between $m_S = -1$ and $m_S = +1$ states becomes partially allowed near GSLAC. This transition can be used to double the spin detection sensitivity (compared with sensitivity obtained using transitions associated with a change in the magnetic quantum number m_S equals +1 or

* eyal@ee.technion.ac.il

–1). However, away from GSLAC, detection based on this transition requires double-quantum driving [27].

II. EXPERIMENTAL SETUP

A diamond sample with nitrogen concentration lower than 200 ppm is electron-irradiated at energy and dose of 2.8 MeV and $8 \times 10^{18} \text{ cm}^{-2}$, respectively, and annealed at 900°C for 2 h to create N-V⁻ defects. The N-V⁻ concentration is $3 \times 10^{17} \text{ cm}^{-3}$. Concentration is estimated by comparing with a reference sample having a known N-V concentration (with sufficiently low laser power, for which fluorescence is proportional to N-V concentration) [33]. The sample assembly is placed at a cryostat with a base temperature of 3.6 K. To reach the GSLAC region, the diamond [111] axis direction is placed nearly parallel to the externally applied static magnetic field, which is generated by superconducting coils.

Two antennas are employed for spin driving. An rf solenoid, having its axis nearly parallel to the applied static magnetic field, allows longitudinal driving, whereas transverse driving is applied using a microwave loop antenna (LA) having its axis nearly orthogonal to the applied static magnetic field. The impedance mismatching coefficient ζ , which is given by $\zeta = \omega L/Z_0$ [34], where ω is the driving angular frequency, L is the antenna's inductance, and $Z_0 = 50 \Omega$ is the impedance of the coaxial cable attached to the antenna, is $\zeta = 94$ for the rf solenoid at $\omega/2\pi = 10 \text{ MHz}$ and $\zeta = 6.0$ for the MW LA at $\omega/2\pi = 3 \text{ GHz}$. An impedance matching capacitor, serially connected to the rf solenoid, is employed for the measurements shown in Fig. 4.

The experimental setup used for performing ODMR measurements is described in Ref. [35]. ODMR signal recorded near the GSLAC region is shown in Fig. 1 as a function of the driving frequency ω and magnetic field B .

III. TRIPLET GROUND STATE

When hyperfine interaction is disregarded, the ground-state spin-triplet Hamiltonian \mathcal{H} becomes [36,37]

$$\frac{\mathcal{H}}{\hbar} = \frac{\omega_D S_z^2}{\hbar^2} + \frac{\omega_E (S_+^2 + S_-^2)}{2\hbar^2} - \frac{\gamma_e \mathbf{B} \cdot \mathbf{S}}{\hbar}, \quad (1)$$

where $\omega_D = 2\pi \times 2.87 \text{ GHz}$ is the zero-field splitting, $\omega_E \ll \omega_D$ is a strain-induced splitting, $\gamma_e = 2\pi \times 28.03 \text{ GHz T}^{-1}$ is the electron spin gyromagnetic ratio, $\mathbf{S} = S_x \hat{x} + S_y \hat{y} + S_z \hat{z}$ is the spin $S = 1$ angular momentum vector operator, and $S_{\pm} = S_x \pm iS_y$. The applied magnetic field is expressed as $\mathbf{B} = \gamma_e^{-1} \boldsymbol{\omega}$, where the angular frequency vector $\boldsymbol{\omega} = (\omega_x, \omega_y, \omega_z) = \boldsymbol{\omega}_{\text{dc}} + \boldsymbol{\omega}_{\text{ac}}$ is decomposed into a static part $\boldsymbol{\omega}_{\text{dc}} = (\omega_{\text{dc},x}, \omega_{\text{dc},y}, \omega_{\text{dc},z})$ (see Fig. 2) and a time-varying part $\boldsymbol{\omega}_{\text{ac}} = (\omega_{\text{ac},x}, \omega_{\text{ac},y}, \omega_{\text{ac},z})$ (having a vanishing averaged value). GSLAC occurs when $\boldsymbol{\omega} \simeq (0, 0, \omega_D)$. The black solid lines in Figs. 1(a2) and

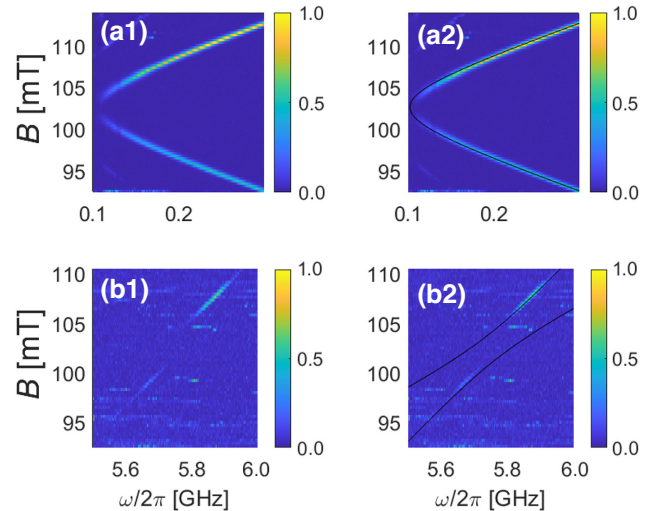


FIG. 1. ODMR in the GSLAC region. The (a) low-frequency and (b) high-frequency resonances. The black solid lines in (a2) and (b2) are based on numerical diagonalization of the triplet Hamiltonian (1).

1(b2) are derived from a numerical diagonalization of the triplet Hamiltonian (1).

IV. RWA

The system's response to both longitudinal and transverse external driving is estimated below using the RWA. The 3×3 matrix representation $H = H_{\text{dc}} + H_{\text{ac}}$ of the Hamiltonian operator \mathcal{H} is decomposed into static H_{dc} and time-varying H_{ac} parts. Two unitary transformations are successively applied to H . The first one is performed

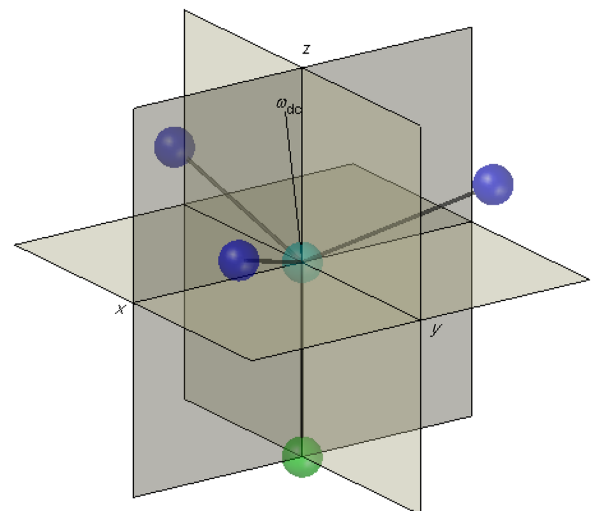


FIG. 2. N-V. The N-V axis is parallel to the z axis, and the static field $\boldsymbol{\omega}_{\text{dc}}$, which is nearly parallel to the z axis, lies in the x - z plane.

with a time-independent unitary matrix U , which diagonalizes the static part, i.e., the 3×3 matrix $U^\dagger H_{\text{dc}} U \equiv H'_{\text{dc}}$ is diagonal. The matrix elements of $\hbar^{-1}H' = \hbar^{-1}U^{-1}HU$ are denoted by $\omega'_{n',n''}$, where $n', n'' \in \{1, 2, 3\}$. The first transformation is explained in Sec. V and in Appendix A.

The second transformation, which is discussed in this section, and which is applied to H' , may help in simplifying the evaluation of the steady-state response of the driven spin system under study. In general, a nonlinear response may give rise to a highly complex steady state. However, in some cases the response is dominated by a single frequency-mixing process. For such cases the RWA can be employed to derive an analytical approximation for the system's steady-state response.

The second transformation is given by $H'' = -i\hbar u^\dagger (du/dt) + u^\dagger H' u$, where the elements $u_{n',n''}$ of the diagonal unitary matrix u are given by $u_{n',n''} = \delta_{n',n''} \exp(-i \int^t dt' \omega'_{n',n'}(t'))$. The matrix elements $\omega''_{n',n''}$ of $\hbar^{-1}H''$ are given by

$$\omega''_{n',n''} = (1 - \delta_{n',n''}) \omega'_{n',n''} e^{-i \int^t dt' (\omega'_{n'',n''}(t') - \omega'_{n',n'}(t'))}. \quad (2)$$

Note that the matrix $\hbar^{-1}H''$ is hollow, i.e., all its diagonal elements $\omega''_{n',n'}$ vanish [see Eq. (2)].

Consider the case where for some $n' \neq n''$ the term $\omega'_{n'',n''} - \omega'_{n',n'}$ in Eq. (2) can be expressed as $\omega'_{n'',n''} - \omega'_{n',n'} = \Omega_0 - \Omega_{L1} \cos(\Omega_L t')$, and the term $\omega'_{n',n''}$ as $\omega'_{n',n''} = \Omega_{T1} e^{i\Omega_T t'}$, where Ω_0 , Ω_{L1} , Ω_L , Ω_{T1} , and Ω_T are all real constants. With the help of the Jacobi-Anger expansion one finds that for this case [see Eq. (2)]

$$\omega''_{n',n''} = \sum_{l=-\infty}^{\infty} \frac{\Omega_{1,l}}{2} e^{-i\Omega_{d,l}t}, \quad (3)$$

where $\Omega_{1,l} = 2\Omega_{T1}J_l(\Omega_{L1}/\Omega_L)$, J_l denotes the Bessel function of the first kind, and $\Omega_{d,l}$, which is given by $\Omega_{d,l} = \Omega_0 - \Omega_T - l\Omega_L$, represents the angular frequency detuning corresponding to the l th frequency-mixing resonance, occurring when $\Omega_T + l\Omega_L = \Omega_0$.

Rapidly oscillating terms are disregarded in the RWA. Consider the case where the matrix elements $\omega''_{n',n''}$ of $\hbar^{-1}H''$ are Fourier expanded as sums of terms having the form $(\Omega_1/2) e^{-i\Omega_{d,l}t}$ [see Eq. (3)], where the driving amplitudes Ω_1 and the frequency detunings Ω_d are real constants. The effect of each such a term is strong when the amplitude $|\Omega_1|$ is large and the detuning $|\Omega_d|$ is small. The analysis is greatly simplified when, among all terms $\omega''_{n',n''}$ in the upper diagonal of $\hbar^{-1}H''$ (i.e., $n' < n''$), a single term having the form $(\Omega_1/2) e^{-i\Omega_{d,l}t}$ in a single matrix element ω''_{n_1,n_2} , where $n_1 < n_2$, dominates (recall that the diagonal elements of H'' vanish). For this case, in the RWA all other terms are disregarded, i.e., it is assumed

that the only nonvanishing matrix elements $\omega''_{n',n''}$ of $\hbar^{-1}H''$ are $\omega''_{n_1,n_2} = (\Omega_1/2) e^{-i\Omega_{d,l}t}$ and $\omega''_{n_2,n_1} = (\Omega_1/2) e^{i\Omega_{d,l}t}$. The effect of driving can be characterized by the coefficient \mathcal{P}_{n_1,n_2} , which is given by [see Eq. (5) of Ref. [38] and Eq. (D11) of Ref. [39]]

$$\mathcal{P}_{n_1,n_2} = \frac{\frac{\Omega_1^2}{\gamma_1 \gamma_2}}{1 + \frac{\Omega_d^2}{\gamma_2^2} + \frac{\Omega_1^2}{\gamma_1 \gamma_2}}, \quad (4)$$

where γ_1 (γ_2) is a longitudinal (transverse) spin relaxation rate. Note that for a two-level system $\mathcal{P} = 1 - P_0/P_s$, where P_0 (P_s) is the population polarization in steady state with (without) driving [see Ref. [40] and Eq. (17.265) of Ref. [41]]. The coefficient \mathcal{P}_{n_1,n_2} can be used to approximately quantify the effect of driving on steady-state ODMR signal.

V. DIAGONALIZATION

Prior to the above-explained transformation that treats the driving terms using the RWA, a time-independent transformation is applied in order to diagonalize the static part of the Hamiltonian H_{dc} . The diagonalized static part of the Hamiltonian reveals the transition frequencies, whereas the unitary matrix that diagonalizes H_{dc} reveals the transition selection rules.

The matrix H is given by [the term $\omega_{zd}/2$ has been added to the diagonal; see Eq. (1)]

$$\frac{H}{\hbar} = \begin{pmatrix} -\frac{\omega_{zd}}{2} & \frac{\omega_\delta}{2} & \omega_E \\ \frac{\omega_\delta^*}{2} & \frac{\omega_{zd}}{2} & \frac{\omega_\delta}{2} \\ \omega_E & \frac{\omega_\delta^*}{2} & \omega_h \end{pmatrix}, \quad (5)$$

where $\omega_{zd} = \omega_z - \omega_D$ represents detuning from GSLAC, $\omega_\delta = -\sqrt{2}(\omega_x - i\omega_y)$ represents transverse magnetic fields, and $\omega_h = (\omega_D + 3\omega_{zd})/2$.

The static part H_{dc} of H [see Eq. (5)] can be expressed as (it is assumed that $\omega_{\text{dc},y} = 0$)

$$\frac{H_{\text{dc}}}{\hbar} = \frac{\omega_{R0}}{2} \begin{pmatrix} -\cos\theta & -\sin\theta & \frac{2\omega_E}{\omega_{R0}} \\ -\sin\theta & \cos\theta & -\frac{\omega_H}{\omega_{R0}} \\ \frac{2\omega_E}{\omega_{R0}} & -\frac{\omega_H}{\omega_{R0}} & \frac{2\omega_{\text{dc},h}}{\omega_{R0}} \end{pmatrix}, \quad (6)$$

where $\omega_{R0} = \sqrt{(\omega_{\text{dc},z} - \omega_D)^2 + \omega_H^2}$, $\omega_H = \sqrt{2}\omega_{\text{dc},x}$, $\omega_{\text{dc},h} = (\omega_D + 3\omega_{\text{dc},z})/2$, and the angle θ is given by

$$\cot\theta = \frac{\omega_{\text{dc},z} - \omega_D}{\omega_H} \equiv \eta. \quad (7)$$

Note that GSLAC corresponds to the case where $\omega_{\text{dc},z} = \omega_D$, $\eta = 0$, and $|\theta| = \pi/2$, whereas $|\eta| \rightarrow \infty$ and $\theta \rightarrow$

0 far from GSLAC. The GSLAC transition angular frequency is approximately given by $\omega_{R0} = \omega_H \sqrt{1 + \eta^2}$.

In the vicinity of the GSLAC, the static part H_{dc} of H is approximately diagonalized using the transformation $H'_{dc} = U^{-1} H_{dc} U$, where the unitary matrix U represents a rotation about the z axis through an angle of $\theta/2$. Applying the same transformation U to the time-dependent part H_{ac} yields two terms: $H'_{ac} = U^{-1} H_{ac} U = H'_{acT} + H'_{acL}$. The first one H'_{acT} , which is given by (see Appendix A)

$$\frac{H'_{acT}}{\hbar} = \begin{pmatrix} -\omega_{TL} & \omega_{TT} & -\frac{\omega_T^* \sin \frac{\theta}{2}}{\sqrt{2}} \\ \omega_T^* & \omega_{TL} & -\frac{\omega_T^* \cos \frac{\theta}{2}}{\sqrt{2}} \\ -\frac{\omega_T \sin \frac{\theta}{2}}{\sqrt{2}} & -\frac{\omega_T \cos \frac{\theta}{2}}{\sqrt{2}} & 0 \end{pmatrix}, \quad (8)$$

where $\omega_{TL} = 2^{-3/2} (\omega_T + \omega_T^*) \sin \theta$, $\omega_{TT} = 2^{-1/2} (\omega_T \sin^2(\theta/2) - \omega_T^* \cos^2(\theta/2))$, and where $\omega_T = \omega_{ac,x} + i\omega_{ac,y}$, originates from transverse driving, whereas longitudinal driving gives rise to the second term H'_{acL} , which is given by (see Appendix A)

$$\frac{H'_{acL}}{\hbar} = \frac{\omega_{ac,z}}{2} \begin{pmatrix} -\cos \theta & \sin \theta & 0 \\ \sin \theta & \cos \theta & 0 \\ 0 & 0 & 3 \end{pmatrix}. \quad (9)$$

Note that $\cos \theta = \eta / \sqrt{\eta^2 + 1}$, $\sin \theta = 1 / \sqrt{\eta^2 + 1}$, and $-\omega_{TL}^2 - \omega_{TT} \omega_{TT}^* = -|\omega_T|^2 / 2$ (determinant of the 2×2 top upper left block of $\hbar^{-1} H'_{acT}$).

VI. SINGLE-ANTENNA DRIVE

The rotation angle $\theta/2$ associated with the diagonalization of the static part H_{dc} (6) [see Eq. (A2)] becomes relatively large near GSLAC. Consequently, in this region the contribution of the MW LA to the effective value of longitudinal driving amplitude becomes significant [see Eq. (8)]. As is demonstrated below (see Fig. 3), this effective longitudinal driving gives rise to a sequence of superharmonic resonances occurring near GSLAC.

The plot in Fig. 3(a) exhibits ODMR measurements performed with a monochromatic driving applied only to the MW LA. The driving has a fixed frequency $\omega_T / (2\pi) = 145$ MHz and a varying power P_T . The driving amplitude, which is denoted by ω_{T1} , is proportional to $P_T^{1/2}$. In the transformed basis (in which the static part of the Hamiltonian is diagonalized), the effective longitudinal (transverse) driving amplitude is ω_{TL} (ω_{TT}) [see Eq. (8)].

The l th frequency-mixing resonance occurs when $\omega_{R0} = \omega_H \sqrt{1 + \eta^2} = l\omega_T$, where l is a positive integer. This resonance condition is graphically displayed in Fig. 3(c). In the experimental data shown in Fig. 3(a), resonances with $l \leq 10$ can be resolved. The driving-induced polarization coefficient \mathcal{P} , which is calculated using Eqs. (3) and (4), is shown in Fig. 3(b). Parameters' assumed values are

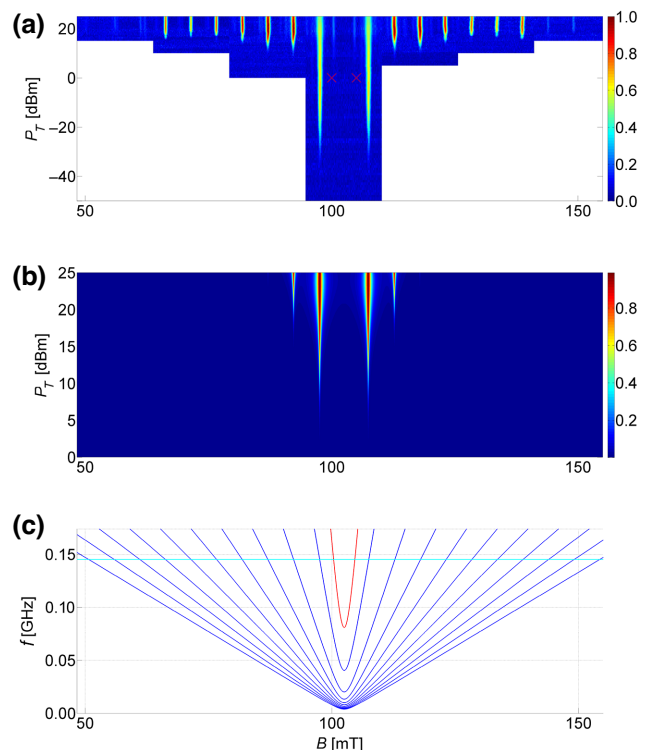


FIG. 3. Single-antenna drive. (a) ODMR signal as a function of static magnetic field B and driving power P_T . (b) Calculated driving-induced polarization coefficient \mathcal{P} [see Eq. (4)]. The parameters' assumed values for the calculation of \mathcal{P} are $\gamma_1 = 0.5$ MHz and $\gamma_2 = 2$ MHz. (c) Graphical representation of the frequency-mixing resonance condition $\omega_{R0} = \omega_H \sqrt{1 + \eta^2} = l\omega_T$. The driving frequency $\omega_T / (2\pi) = 145$ MHz is represented by the horizontal cyan line.

listed in the caption of Fig. 3. The comparison between the measured ODMR signal [Fig. 3(a)] and calculated polarization coefficient \mathcal{P} [Fig. 3(b)] suggests that the decay of resonance intensity with $|l|$ is theoretically overestimated. The discrepancy is mainly attributed to dipolar coupling, which gives rise to an additional driving term, which is disregarded in the calculation of \mathcal{P} [42–45].

The two resonances labeled in Fig. 3(a) by red cross symbols represent second Larmor lines. The resonance condition for the second Larmor lines, which is given by $2\omega_{R0} = \omega_T$, is graphically shown in Fig. 3(c) (the term $2\omega_{R0}$ is represented by the red hyperbola, and $\omega_T / (2\pi) = 145$ MHz by the horizontal cyan line). Note that the nonlinear process responsible for the second Larmor lines is not taken into account in the calculation of the driving-induced polarization coefficient \mathcal{P} [see Fig. 3(b)].

VII. TWO-ANTENNA DRIVE

The case of simultaneous driving with both rf solenoid and MW LA is exhibited by the plots shown in

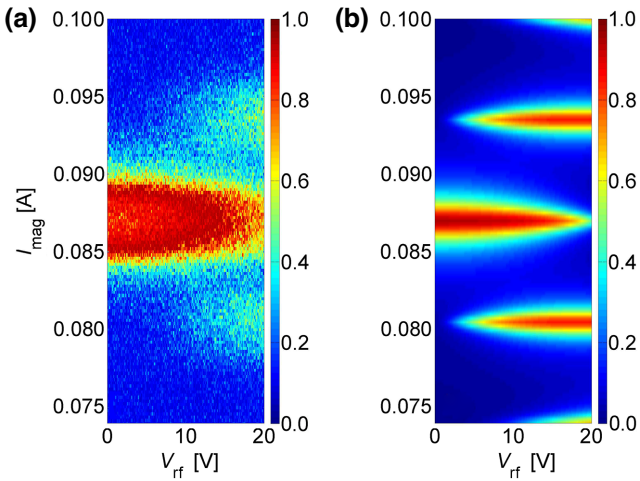


FIG. 4. Two-antenna drive. (a) ODMR signal as a function of rf solenoid applied voltage amplitude V_{rf} and current applied to the solenoid generating the static magnetic field I_{mag} . The fixed rf solenoid driving frequency is $\Omega_L/(2\pi) = 10.5$ MHz, MW LA driving amplitude is $\Omega_{T1} = 5.6$ MHz, and MW LA driving frequency is $\Omega_T/(2\pi) = 3.15$ GHz. (b) Calculated driving-induced polarization coefficient \mathcal{P} [see Eq. (4)]. The parameters' assumed values for the calculation of \mathcal{P} are $\gamma_1 = 0.5$ MHz and $\gamma_2 = 2$ MHz.

Figs. 4 and 5, which demonstrate that frequency mixing between off-resonance monochromatic driving tones can be employed for resonance driving. This frequency-mixing process is related to the Landau-Zener-Stückelberg effect, which describes a coherent interference occurring in a two-level system under two simultaneously applied driving tones [46]. Landau-Zener-Stückelberg interferometry (see Fig. 4) commonly requires intense longitudinal driving. For exploring this interferometry, a capacitor having capacitance of $36 \mu\text{F}$ is serially connected to the rf solenoid. The added capacitor helps in enhancing the magnetic field driving amplitude by suppressing the undesirable effect of parasitic capacitance of the rf solenoid. The rf solenoid with the added capacitor is operated near its resonance frequency of 10.5 MHz.

For the ODMR signal shown in the plot in Fig. 4(a), the rf solenoid is driven with a varying amplitude Ω_{L1} (proportional to the applied voltage amplitude V_{rf}) and a fixed frequency of $\Omega_L/(2\pi) = 10.5$ MHz, and the MW LA is driven with a fixed amplitude of $\Omega_{T1} = 5.6$ MHz and a fixed frequency of $\Omega_T/(2\pi) = 3.15$ GHz. The plot shown in Fig. 4(b) displays the calculated polarization coefficient \mathcal{P} [see Eq. (4)] in the same region, as a function of V_{rf} and the current I_{mag} applied to the solenoid generating the static magnetic field. The assumed parameters' values used for the calculation of \mathcal{P} , which is based on Eqs. (3) and (4), are listed in the caption of Fig. 4.

While the measurements presented in Fig. 4 have been performed away from the GSLAC, the case of two-antenna

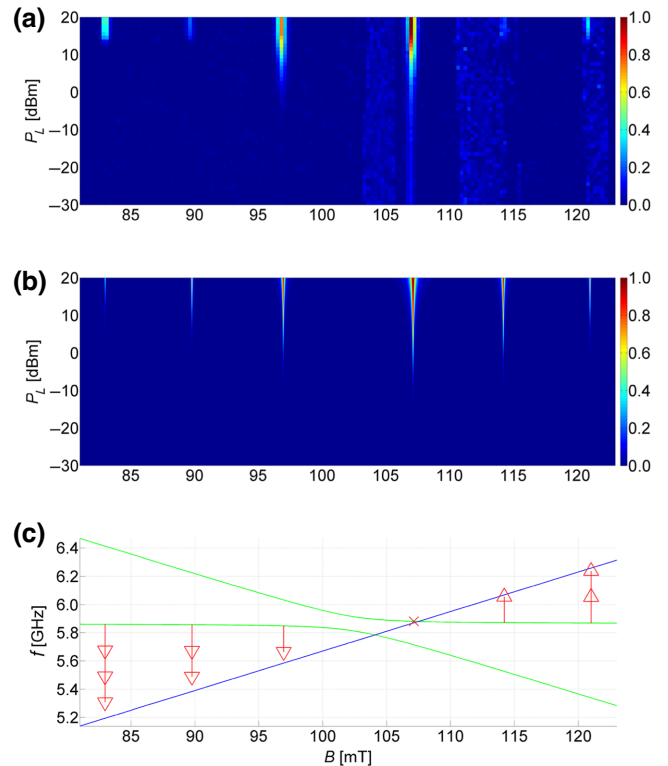


FIG. 5. Two-antenna drive near GSLAC. (a) ODMR signal as a function of static magnetic field B and rf solenoid driving power P_L , with a fixed rf solenoid driving frequency of $\omega_L/(2\pi) = 185$ MHz, MW LA driving frequency of $\omega_T/(2\pi) = 5.87$ GHz, and MW LA driving power of 25 dBm. (b) The calculated polarization coefficient \mathcal{P} [see Eq. (4)]. (c) Graphical representation of the frequency-mixing matching condition.

driving near GSLAC is demonstrated by the plots shown in Fig. 5. The plot in Fig. 5(a) displays ODMR data as a function of static magnetic field B and rf solenoid driving power P_L . For this measurement, the rf solenoid driving frequency is $\omega_L/(2\pi) = 185$ MHz, MW LA driving frequency is $\omega_T/(2\pi) = 5.87$ GHz, and MW LA driving power is 25 dBm. The plot shown in Fig. 5(b) displays the calculated polarization coefficient \mathcal{P} in the same region [see Eqs. (3) and (4)].

The calculated energy eigenvalues of the triplet Hamiltonian (1) are plotted as a function of B in Fig. 5(c). To graphically display the frequency-mixing matching condition, the two lowest eigenenergies [green solid lines in Fig. 5(c)] are vertically shifted upwards by the MW LA driving frequency $\omega_T/(2\pi) = 5.87$ GHz. The highest eigenenergy is represented by the solid blue line. The length of the red vertical arrows in Fig. 5(c) is the rf solenoid driving frequency $\omega_L/(2\pi) = 185$ MHz.

VIII. SUMMARY

Nonlinear magnetic resonance sensing of N-V⁻ defects at low temperatures is demonstrated using ODMR. Several

frequency-mixing configurations are employed, including Landau-Zener-Stückelberg interferometry and two-tone driving spectroscopy. Magnetic driving is applied in the longitudinal and transverse directions using MW and rf fields. The experimental results are compared with prediction of theoretical analysis based on the RWA.

Frequency mixing offers some advantages for sensing applications, including the ability to eliminate crosstalk between driving and detection. This crosstalk problem is important for cavity-based detection of magnetic resonance [2]. At cryogenic temperatures, the method of frequency mixing can be used for applications such as magnetometry of superconducting materials [47]. In this work, ODMR has been employed for exploring the efficiency of a variety of frequency-mixing driving configurations. Future study will explore and optimize protocols for cavity-based spin spectroscopy that are based on frequency mixing.

ACKNOWLEDGMENTS

This work is supported by the Israeli Science Foundation and the Israeli Ministry of Science.

APPENDIX A: DERIVATION OF EQS. (8) AND (9)

The approximate diagonalization of the static part H_{dc} (6) of H in the vicinity of the GSLAC is based on the relation

$$U^{-1} \begin{pmatrix} -\cos \theta & -\sin \theta & 0 \\ -\sin \theta & \cos \theta & 0 \\ 0 & 0 & 1 \end{pmatrix} U = \begin{pmatrix} -1 & 0 & 0 \\ 0 & 1 & 0 \\ 0 & 0 & 1 \end{pmatrix}, \quad (\text{A1})$$

where the unitary matrix U , which is given by

$$U = \begin{pmatrix} \cos \frac{\theta}{2} & -\sin \frac{\theta}{2} & 0 \\ \sin \frac{\theta}{2} & \cos \frac{\theta}{2} & 0 \\ 0 & 0 & 1 \end{pmatrix}, \quad (\text{A2})$$

represents a rotation about the z axis through an angle of $\theta/2$. The derivation of Eqs. (8) and (9) is performed using the following matrix relations:

$$U^{-1} \begin{pmatrix} -1 & 0 & 0 \\ 0 & 1 & 0 \\ 0 & 0 & 0 \end{pmatrix} U = \begin{pmatrix} -\cos \theta & \sin \theta & 0 \\ \sin \theta & \cos \theta & 0 \\ 0 & 0 & 0 \end{pmatrix}, \quad (\text{A3})$$

$$U^{-1} \begin{pmatrix} 0 & 1 & 0 \\ 1 & 0 & 0 \\ 0 & 0 & 0 \end{pmatrix} U = \begin{pmatrix} \sin \theta & \cos \theta & 0 \\ \cos \theta & -\sin \theta & 0 \\ 0 & 0 & 0 \end{pmatrix}, \quad (\text{A4})$$

$$U^{-1} \begin{pmatrix} 0 & 0 & 1 \\ 0 & 0 & 0 \\ 1 & 0 & 0 \end{pmatrix} U = \begin{pmatrix} 0 & 0 & \cos \frac{\theta}{2} \\ 0 & 0 & -\sin \frac{\theta}{2} \\ \cos \frac{\theta}{2} & -\sin \frac{\theta}{2} & 0 \end{pmatrix}, \quad (\text{A5})$$

$$U^{-1} \begin{pmatrix} 0 & 0 & 0 \\ 0 & 0 & 1 \\ 0 & 1 & 0 \end{pmatrix} U = \begin{pmatrix} 0 & 0 & \sin \frac{\theta}{2} \\ 0 & 0 & \cos \frac{\theta}{2} \\ \sin \frac{\theta}{2} & \cos \frac{\theta}{2} & 0 \end{pmatrix}, \quad (\text{A6})$$

and

$$\begin{aligned} U^{-1} & \begin{pmatrix} 0 & x+iy & 0 \\ x-iy & 0 & x+iy \\ 0 & x-iy & 0 \end{pmatrix} U \\ &= \begin{pmatrix} x \sin \theta & x \cos \theta + iy & (x+iy) \sin \frac{\theta}{2} \\ x \cos \theta - iy & -x \sin \theta & (x+iy) \cos \frac{\theta}{2} \\ (x-iy) \sin \frac{\theta}{2} & (x-iy) \cos \frac{\theta}{2} & 0 \end{pmatrix}. \end{aligned} \quad (\text{A7})$$

- [1] Tatsuma Yamaguchi, Yuichiro Matsuzaki, Shiro Saito, Soya Saijo, Hideyuki Watanabe, Norikazu Mizuochi, and Junko Ishi-Hayase, Bandwidth analysis of ac magnetic field sensing based on electronic spin double-resonance of nitrogen-vacancy centers in diamond, *Jpn. J. Appl. Phys.* **58**, 100901 (2019).
- [2] Nir Alfasi, Sergei Masis, Roni Winik, Demitry Farfurnik, Oleg Shtempluck, Nir Bar-Gill, and Eyal Buks, Exploring the nonlinear regime of light-matter interaction using electronic spins in diamond, *Phys. Rev. A* **97**, 063808 (2018).
- [3] A. Bienfait, P. Campagne-Ibarcq, A. H. Kiilerich, X. Zhou, S. Probst, J. J. Pla, T. Schenkel, D. Vion, Daniel Estève, J. J. L. Morton, *et al.*, Magnetic resonance with squeezed microwaves, *Phys. Rev. X* **7**, 041011 (2017).
- [4] Roei Levi, Sergei Masis, and Eyal Buks, Instability in the Hartmann-Hahn double resonance, *Phys. Rev. A* **102**, 053516 (2020).
- [5] Daniel Gottesman, Alexei Kitaev, and John Preskill, Encoding a qubit in an oscillator, *Phys. Rev. A* **64**, 012310 (2001).
- [6] Ivar Martin, Gil Refael, and Bertrand Halperin, Topological frequency conversion in strongly driven quantum systems, *Phys. Rev. X* **7**, 041008 (2017).
- [7] André Eckardt and Egidijus Anisimovas, High-frequency approximation for periodically driven quantum systems from a Floquet-space perspective, *New J. Phys.* **17**, 093039 (2015).
- [8] N. B. Manson, L. J. Rogers, Elena Alexandrovna Wilson, and Changjiang Wei, Hole burning-EIT studies of the NV centre in diamond, *J. Lumin.* **130**, 1659 (2010).
- [9] Pauli Kehayias, Mariusz Mrózek, Victor M. Acosta, A. Jarmola, D. S. Rudnicki, Ron Folman, Wojciech Gawlik, and Dmitry Budker, Microwave saturation spectroscopy of

- nitrogen-vacancy ensembles in diamond, *Phys. Rev. B* **89**, 245202 (2014).
- [10] William D. Oliver and Sergio O. Valenzuela, Large-amplitude driving of a superconducting artificial atom: Interferometry, cooling, and amplitude spectroscopy, *Quantum Inf. Process.* **8**, 261 (2009).
- [11] Marcus W. Doherty, Neil B. Manson, Paul Delaney, Fedor Jelezko, Jörg Wrachtrup, and Lloyd C. L. Hollenberg, The nitrogen-vacancy colour centre in diamond, *Phys. Rep.* **528**, 1 (2013).
- [12] L. Rondin, J. P. Tetienne, T. Hingant, J. F. Roch, P. Maletinsky, and V. Jacques, Magnetometry with nitrogen-vacancy defects in diamond, *Rep. Prog. Phys.* **77**, 056503 (2014).
- [13] Siddharth Dhomkar, Jacob Henshaw, Harishankar Jayakumar, and Carlos A. Meriles, Long-term data storage in diamond, *Sci. Adv.* **2**, e1600911 (2016).
- [14] Xiaobo Zhu, Shiro Saito, Alexander Kemp, Kosuke Kakuyanagi, Shin-ichi Karimoto, Hayato Nakano, William J. Munro, Yasuhiro Tokura, Mark S. Everitt, Kae Nemoto, *et al.*, Coherent coupling of a superconducting flux qubit to an electron spin ensemble in diamond, *Nature* **478**, 221 (2011).
- [15] Yuimaru Kubo, Cecile Grezes, Andreas Dewes, T. Ueda, Junichi Isoya, H. Sumiya, N. Morishita, H. Abe, S. Onoda, T. Ohshima, *et al.*, Hybrid quantum circuit with a superconducting qubit coupled to a spin ensemble, *Phys. Rev. Lett.* **107**, 220501 (2011).
- [16] R. Amsüss, Ch. Koller, T. Nöbauer, S. Putz, S. Rotter, K. Sandner, S. Schneider, M. Schramböck, G. Steinhauser, H. Ritsch, J. Schmiedmayer, and J. Majer, Cavity QED with magnetically coupled collective spin states, *Phys. Rev. Lett.* **107**, 060502 (2011).
- [17] C. Grezes, Brian Julsgaard, Y. Kubo, M. Stern, T. Ueda, J. Isoya, H. Sumiya, H. Abe, S. Onoda, T. Ohshima, *et al.*, Multimode storage and retrieval of microwave fields in a spin ensemble, *Phys. Rev. X* **4**, 021049 (2014).
- [18] Jonathan D. Breeze, Enrico Salvadori, Juna Sathian, Neil McN Alford, and Christopher W. M. Kay, Continuous-wave room-temperature diamond maser, *Nature* **555**, 493 (2018).
- [19] Thomas Wolf, Philipp Neumann, Kazuo Nakamura, Hitoshi Sumiya, Takeshi Ohshima, Junichi Isoya, and Jörg Wrachtrup, Subpicotesla diamond magnetometry, *Phys. Rev. X* **5**, 041001 (2015).
- [20] Scott T. Alsid, Jennifer M. Schloss, Matthew H. Steinecker, John F. Barry, Andrew C. Maccabe, Guoqing Wang, Paola Cappellaro, and Danielle A. Braje, Solid-state microwave magnetometer with picotesla-level sensitivity, *Phys. Rev. Appl.* **19**, 054095 (2023).
- [21] Guoqing Wang, Yi-Xiang Liu, Jennifer M. Schloss, Scott T. Alsid, Danielle A. Braje, and Paola Cappellaro, Sensing of arbitrary-frequency fields using a quantum mixer, *Phys. Rev. X* **12**, 021061 (2022).
- [22] A. K. Dmitriev, H. Y. Chen, G. D. Fuchs, and A. K. Vershovskii, Dual-frequency spin-resonance spectroscopy of diamond nitrogen-vacancy centers in zero magnetic field, *Phys. Rev. A* **100**, 011801 (2019).
- [23] Alexander K. Dmitriev and Anton K. Vershovskii, High-contrast two-frequency optically detected resonances in diamond nitrogen-vacancy centers for timekeeping schemes, *IEEE Sens. Lett.* **4**, 1 (2020).
- [24] A. K. Dmitriev and A. K. Vershovskii, Radio-frequency response of the optically detected level anticrossing signal in nitrogen-vacancy color centers in diamond in zero and weak magnetic fields, *Phys. Rev. A* **105**, 043509 (2022).
- [25] Lilian Childress and Jean McIntyre, Multifrequency spin resonance in diamond, *Phys. Rev. A* **82**, 033839 (2010).
- [26] Hannah Clevenson, Edward H. Chen, Florian Dolde, Carson Teale, Dirk Englund, and Danielle Braje, Diamond-nitrogen-vacancy electronic and nuclear spin-state anti-crossings under weak transverse magnetic fields, *Phys. Rev. A* **94**, 021401 (2016).
- [27] H. J. Mamin, M. H. Sherwood, M. Kim, C. T. Rettner, K. Ohno, D. D. Awschalom, and D. Rugar, Multipulse double-quantum magnetometry with near-surface nitrogen-vacancy centers, *Phys. Rev. Lett.* **113**, 030803 (2014).
- [28] Jingwei Zhou, Pu Huang, Qi Zhang, Zixiang Wang, Tian Tan, Xiangkun Xu, Fazhan Shi, Xing Rong, S. Ashhab, and Jiangfeng Du, Observation of time-domain Rabi oscillations in the Landau-Zener regime with a single electronic spin, *Phys. Rev. Lett.* **112**, 010503 (2014).
- [29] Pu Huang, Jingwei Zhou, Fang Fang, Xi Kong, Xiangkun Xu, Chenyong Ju, and Jiangfeng Du, Landau-Zener-Stückelberg interferometry of a single electronic spin in a noisy environment, *Phys. Rev. X* **1**, 011003 (2011).
- [30] Takumi Mikawa, Ryusei Okaniwa, Yuichiro Matsuzaki, Norio Tokuda, and Junko Ishi-Hayase, Electron-spin double resonance of nitrogen-vacancy centers in diamond under a strong driving field, *Phys. Rev. A* **108**, 012610 (2023).
- [31] V. Jacques, P. Neumann, J. Beck, M. Markham, D. Twitchen, J. Meijer, F. Kaiser, G. Balasubramanian, F. Jelezko, and J. Wrachtrup, Dynamic polarization of single nuclear spins by optical pumping of nitrogen-vacancy color centers in diamond at room temperature, *Phys. Rev. Lett.* **102**, 057403 (2009).
- [32] G. D. Fuchs, Guido Burkard, P. V. Klimov, and D. D. Awschalom, A quantum memory intrinsic to single nitrogen-vacancy centres in diamond, *Nat. Phys.* **7**, 789 (2011).
- [33] D. Farfurnik, N. Alfasi, S. Masis, Y. Kauffmann, E. Farchi, Y. Romach, Y. Hovav, E. Buks, and N. Bar-Gill, Enhanced concentrations of nitrogen-vacancy centers in diamond through TEM irradiation, *Appl. Phys. Lett.* **111**, 123101 (2017).
- [34] D. M. Pozar, *Microwave Engineering* (John Wiley and sons, 1998).
- [35] Nir Alfasi, Sergei Masis, Oleg Shtempluck, and Eyal Buks, Detection of paramagnetic defects in diamond using off-resonance excitation of NV centers, *Phys. Rev. B* **99**, 214111 (2019).
- [36] Preeti Ovartchaiyapong, Kenneth W. Lee, Bryan A. Myers, and Ania C. Bleszynski Jayich, Coherent strain-mediated coupling of a single diamond spin to a mechanical resonator, *ArXiv:1403.4173* (2014).
- [37] E. R. MacQuarrie, T. A. Gosavi, N. R. Jungwirth, S. A. Bhave, and G. D. Fuchs, Mechanical spin control of nitrogen-vacancy centers in diamond, *Phys. Rev. Lett.* **111**, 227602 (2013).

- [38] D. M. Berns, W. D. Oliver, S. O. Valenzuela, A. V. Shytov, K. K. Berggren, L. S. Levitov, and T. P. Orlando, Coherent quasiclassical dynamics of a persistent current qubit, *Phys. Rev. Lett.* **97**, 150502 (2006).
- [39] Eyal Buks, Chunqing Deng, Jean-Luc F. X. Orgazzi, Martin Otto, and Adrian Lupascu, Superharmonic resonances in a strongly coupled cavity-atom system, *Phys. Rev. A* **94**, 033807 (2016).
- [40] Charles P. Slichter, *Principles of Magnetic Resonance* (Springer Science & Business Media, 2013), Vol. 1.
- [41] Eyal Buks, Quantum mechanics - Lecture Notes, <http://buks.net.technion.ac.il/teaching/> (2023).
- [42] A. G. Anderson, Nuclear spin absorption spectra in solids, *Phys. Rev.* **125**, 1517 (1962).
- [43] Hung Cheng, Spin absorption of solids, *Phys. Rev.* **124**, 1359 (1961).
- [44] L. J. F. Broer, On the theory of paramagnetic relaxation, *Physica* **10**, 801 (1943).
- [45] J. T. Daycock and G. Parry Jones, Subsidiary resonances in nuclear magnetic resonance, *J. Phys. C: Solid State Phys.* **2**, 998 (1969).
- [46] S. N. Shevchenko, S. Ashhab, and F. Nori, Landau-Zener-Stückelberg interferometry, *Phys. Rep.* **492**, 1 (2010).
- [47] Nir Alfasi, Sergei Masis, Oleg Shtempeluk, Valleri Kochetok, and Eyal Buks, Diamond magnetometry of Meissner currents in a superconducting film, *AIP Adv.* **6**, 075311 (2016).